Luoshan Wang, Tushar Kumeria, Abel Santos, Peter Forward, Martin F. Lambert, and Dusan Losic

**Iron oxide nanowires from bacteria biofilm as an edfficient visible-light magnetic photocatalyst**

ACS Applied Materials & Interfaces, 2016; 8(31):20110-20119

# Iron Oxide Nanowires from Bacteria Biofilm as Efficient Visible-Light Magnetic Photocatalyst

*Luoshan Wang,[a§] Tushar Kumeria,[a§] Abel Santos,[a] Peter Forward[b], Martin F. Lambert,[c*] Dusan Losic[a*]*

[a] School of Chemical Engineering, The University of Adelaide, Adelaide, SA 5005, Australia.

[b] South Australian (SA) Water, Adelaide, SA-5005, Australia.

[c] School of Civil, Environmental and Mining Engineering, The University of Adelaide, Adelaide SA 5005, Australia.

* E-mail dusan.losic@adelaide.edu.au
* E-mail: mlambert@civeng.adelaide.edu.au

KEYWORDS: Iron oxide nanowires; Bacteria Biofilm; Rhodamine B; visible-light photocatalysis; natural nanostructure

ABSTRACT: Naturally produced iron oxide nanowires by *Mariprofundus ferrooxydans* bacteria as biofilm are evaluated for their structural, chemical, and photocatalytic performance under visible light irradiation. The crystal phase structure of this unique natural material presents 1-dimensional (1D) nanowires like geometry, which is transformed from amorphous to crystalline (hematite) by thermal annealing at high temperatures without of changing their morphology. This study systematically assesses the effect of different annealing temperatures on the photocatalytic activity of iron oxide nanowires produced by *Mariprofundus ferrooxydans* bacteria. The nanowires processed at 800 °C were the most optimal for photocatalytic applications degrading a model dye (Rhodamine B) in less than an hour. These nanowires displayed excellent reusability with no significant loss of activity even after 6 cycles. Kinetic studies by using hydrogen peroxide (radical generator) and isopropyl alcohol (radical scavenger) suggest that OH• is the dominant photooxidant. These nanowires are naturally produced, inexpensive, highly active, stable, and magnetic with the potential to be used for broad applications including environmental remediation, water disinfection and industrial catalysis.

## 1. INTRODUCTION

Photocatalysis is an important process for environmental remediation, industrial production, water splitting and hydrogen generation, and several others.[1-2] So far, titanium dioxide ($TiO_2$) based catalytic materials (i.e. titanium dioxide in different forms and its composites) have been leading this field due to their superior photocatalytic performance.[3-8] However, the practical application of $TiO_2$ based catalytic materials is largely restricted by its relatively wide band-gap (i.e. 3.2 eV).[9-12] Notice that, due to this wide band-gap, only the high energy light (i.e. ultra-violet: UV) is efficiently absorbed by $TiO_2$ catalysts and utilized in carrying out the catalytic reaction. It is worthwhile mentioning here that UV only constitutes approximately 4 % of the solar spectrum, whereas around 50 % and 46 % of the solar light falls in the visible and infra-red (IR) regions of the spectrum, respectively.[13-14] As a result, titanium dioxide based catalytic materials cannot utilize the majority of the solar spectrum for photocatalytic processes. Therefore, the focus of the photocatalysis research has recently shifted towards designing, synthesizing and exploring new catalytic materials that can absorb and utilize efficiently light within the visible region (i.e. 400 to 700 nm) of the spectrum for photocatalytic processes. In the last decade, a number of materials including mixture or doped composites of titanium dioxide with other oxides (i.e. iron oxide, zinc oxide etc.), noble metals and others have been studied.[15-21]

Recently, iron oxide based materials, especially in the nanoparticle forms, have gained significant attention and become attractive material for visible-light photocatalysis. Also, composites of iron oxide and titanium dioxide have gained interest as they can harness both ultraviolet and visible parts of the solar spectrum efficiently. Iron oxide based materials are promising for photocatalysis application due to their low cost, strong adsorption capacity, enhanced stability, and easy recovery using an external magnetic field. The ability of iron oxide

as an efficient photocatalyst has been demonstrated in both laboratory and field scale tests. The pronounced photocatalytic activity of iron oxide, especially $Fe_2O_3$, is due to its band-gap of 2.2 eV, which enables this material to act as an n-type semiconductor with a narrow band-gap. So far, a number of synthetic iron oxide based catalytic systems have been demonstrated in the literature (e.g. $Fe_2O_3$ coated nano pillars and particles).[22-28] Typically, synthetic iron oxide nanomaterials are prepared by a wide variety of synthetic methods including co-precipitation, chemical reduction, hydrothermal process, and so on. However, there are some problems with these methods because of their scalability, high-cost, sustainability and large environmental footprints as they use toxic materials and lead to the generation of toxic chemical waste. Therefore, there is a strong demand to source photocatalysts using more environmentally friendly and scalable processes and the best option is to consider naturally produced materials and resources.

Fortunately, some living organisms have acquired the ability to produce nanostructure with intricate designs and precisely controlled morphologies and dimensions. Among them, several type of bacteria and fungi are known to have the ability to create metallic and metal oxide nanoparticles.[29-34] For example, long and helical iron (II) encrusted nanowires are produced by the zetaproteobacteria, *Mariprofundus ferrooxydans* in an iron abundant environment.[35-36] These nanowires are found in the form of biofilm deposits in the pipe-line system that is used to pump out the saline ground water entering into the River Murray, South Australia, Australia. The bore system has had frequent problems with a significant iron biofilm growth, which causes a substantial cost in regular cleaning of the bores and the resulting biofilm waste material being treated as a waste product. A microscopic investigation revealed that this biofilm waste is composed of helically entangled nanowires, primarily composed of Fe (II)

oxide. This material was explored for several applications due to their interesting 1D nanostructure and chemical nature. One application was photocatalysis and the nanowire proved to be highly efficient light activated reaction mediators (i.e. photocatalysts), which is presented in this study.

In this study we investigate the photocatalytic activity of this bacteria biofilm waste material (i.e. bacteria nanowires, Bac-FeOxNWs) for the degradation of a model organic molecule (i.e. Rhodamine B) as a function of the annealing temperature, pH, different additives, and concentrations of Bac-FeOxNWs and target dye (Rhodamine B). First, the bacteria biofilm were annealed at three different temperatures (600, 800, and 1000 °C) and non-annealed biofilm was used as a control. All the Bac-FeOxNWs samples were subsequently characterized using an array of analytical techniques as scanning electron microscopy (SEM), transmission electron microscopy (TEM), UV-Vis spectroscopy, dynamic light scattering with zeta-potential (DLS), X-ray diffraction spectroscopy (XRD) and others to understand their morphological and chemical properties. The catalytic performance of these Bac-FeOxNWs was evaluated by measuring their efficiency to catalytically decompose Rhodamine B (i.e. a textile dye) under visible light irradiation.

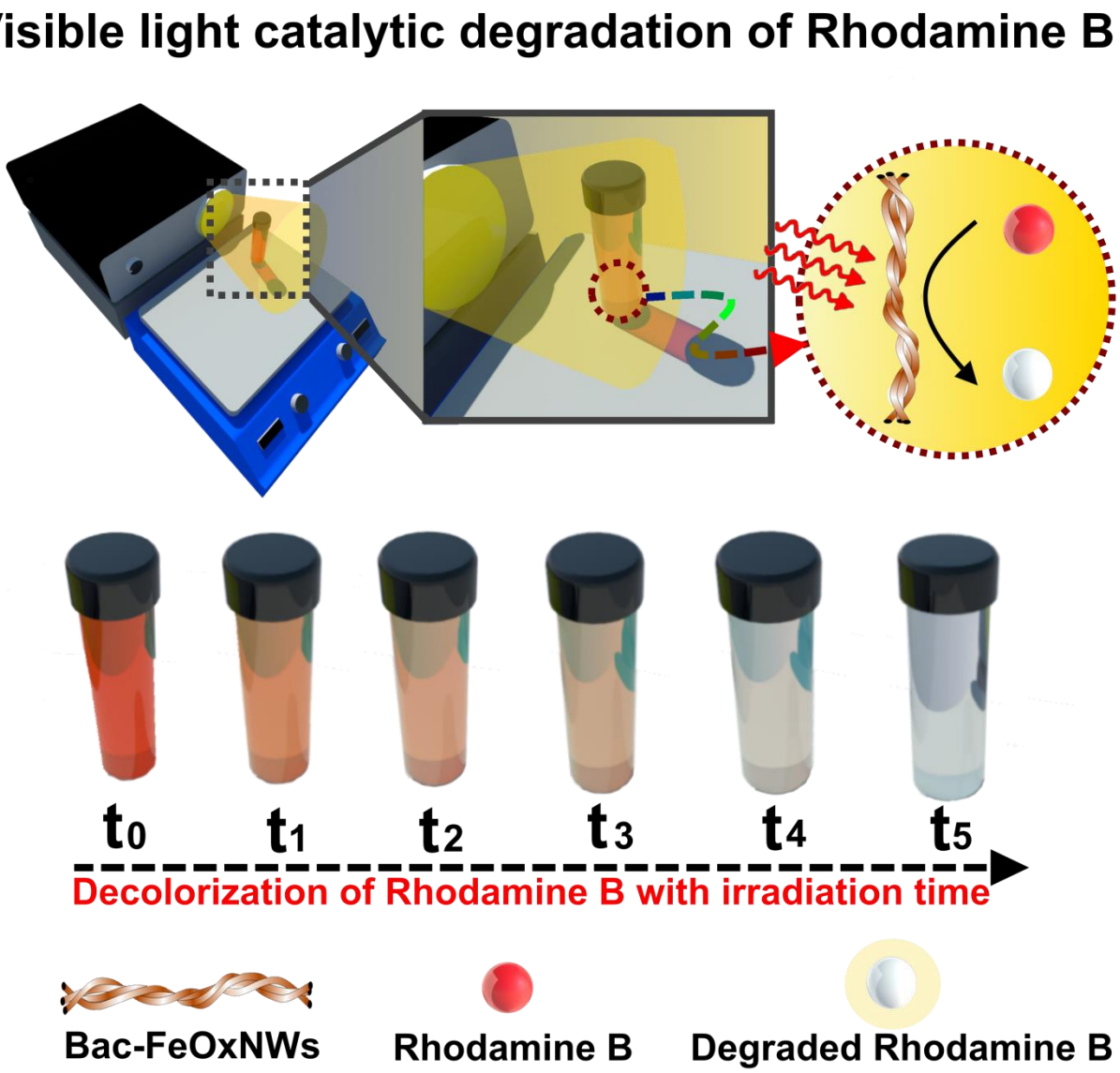


**Scheme 1.** Schematic illustration showing the setup used for degradation RhB in the presence of Bac-FeOxNWs photocatalysts. The top half of the figure shows the setup with a light source (150 W halogen lamp with UV filter) irradiating a mixture of Bac-FeOxNWs and RhB that results in discoloration of RhB indicating efficient photocatalytic degradation. The bottom half of the scheme shows the time course discoloration of RhB in the presence of Bac-FeOxNWs and visible light.

## 2. EXPERIMENTAL SECTION

**2.1. Materials.** Bacterial biofilm was provided by SA Water (South Australia). Rhodamine B ($C_{28}H_{31}CIN_{203}$) powder, hydrogen peroxide (30 % *w*/*w*), hydrochloric acid (39 %, HCl), and sodium hydroxide pellets (98 % *w*/*w*, NaOH) were supplied by Sigma Aldrich (Australia). Ultrapure mili-Q water (18.2 MΩ) (Option-Q, Purelabs, Australia) was used to prepare all solutions used throughout this study.

**2.2. Bac-FeOxNWs purification and annealing.** The collected biofilm samples were suspended in mili-Q water at 1:40 *w*/*v* ratio (i.e. 1 g biofilm in 40 mL of water) and vortexed for 10 minutes to obtain a good suspension. This suspension was subjected to repeated centrifugation at 4200 rpm for 15 min and re-suspension until the conductivity (Thermo Scientific, Orion Star A212, Australia) of the sample reached that of mili-Q water itself, indicating effective removal of salt impurities. This purified biofilm sample was dried in air at 70 °C. A specific amount of the purified biofilm sample, referred to as Bac-FeOxNWs, (100 mg in this case) was subsequently loaded in a silica boat and annealed at three different temperatures including 600, 800, and 1000 ˚C in a tube furnace (Brother Furnace, China) fitted with a quartz tube. **Table 1** summarizes the preparation conditions of all the Bac-FeOxNWs (i.e. name, annealing temperature, and color) and a schematic of the shape and morphology of samples after annealing at different temperatures is included in **Scheme 2**. The annealed samples of biofilm (i.e. Bac-FeOxNWs-600, Bac-FeOxNWs-800, and Bac-FeOxNWs-1000) were washed once more with mili-Q water after thermal annealing, air dried at 70 °C in oven and stored under inert atmosphere until further use.

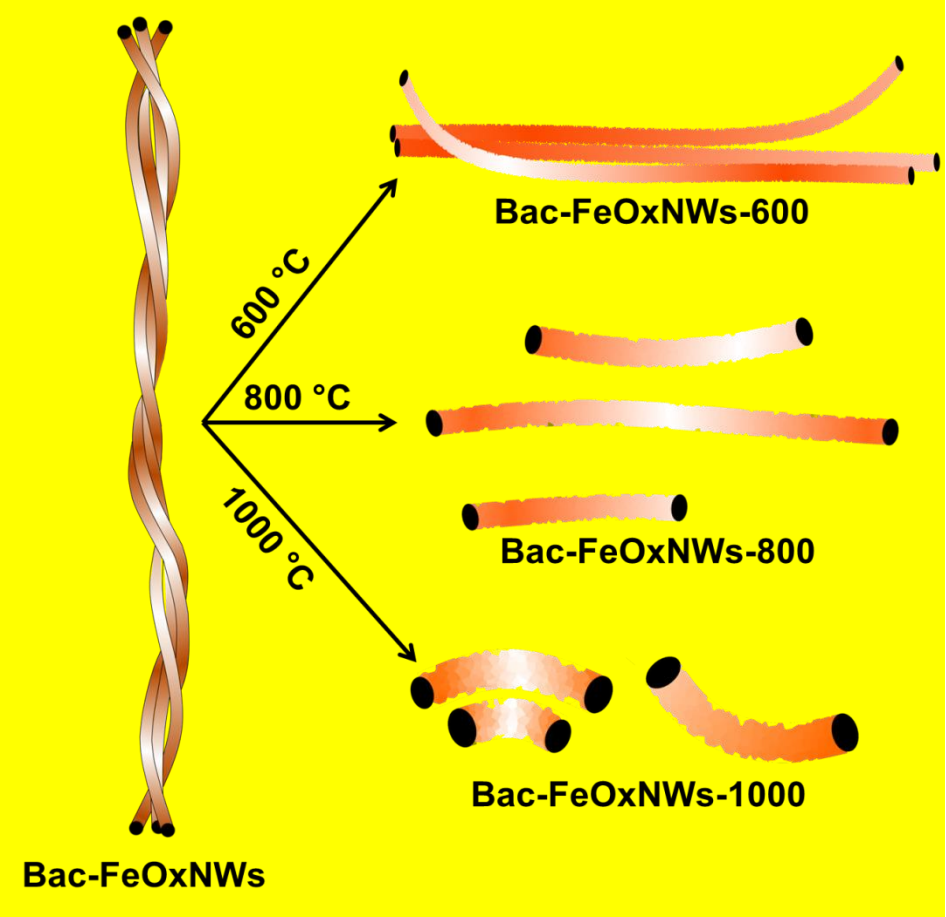


**Scheme 2.** A cartoon illustration showing the shape and morphology of Bac-FeOxNWs at different annealing temperatures.

**2.3. Structural and chemical characterization of Bac-FeOxNWs.** All the prepared Bac-FeOxNWs samples (i.e. Bac-FeOxNWs, Bac-FeOxNWs-600, Bac-FeOxNWs-800, Bac-FeOxNWs-1000) were characterized using scanning electron microscopy (SEM, FEI Quanta 450 FEG-SEM, USA), energy-dispersive X-ray spectroscopy (EDX), X-ray diffraction (XRD, Rigaku MiniFlex 600, Japan), Fourier transform IR (FTIR) spectroscopy (Nicolet 6700 Thermo Fisher, Australia). The particle size and zeta potential were measured using dynamic light scattering (ZetaSizer Nano, Malvern Instruments Ltd., Worcestershire, UK).

**2.4. Visible-light photocatalytic degradation of Rhodamine B.** Photodegradation of Rhodamine B (RhB) was carried out by illuminating the samples using a custom built 150 W white light halogen lamp fitted with a UV filter (high-pass filter with cutoff at 420 nm). Prior to RhB degradation experiment, 2940 µL of mili-Q water and 50 µL of RhB (1 mM) added to a transparent vial containing a specific amount of Bac-FeOxNWs and kept in dark for 24 hours to reach the adsorption-desorption equilibrium. Next day, 10 µL of hydrogen peroxide ($H_2O_2$) was added to the vial and exposed to visible light for 3 h. During this exposure time, the UV-Visible spectrum was recorded every 15 min using a miniature fiber optic spectrometer equipped with a tungsten lamp (USB 4000 and LS1-LL light source respectively, Ocean Optics USA). In this regard, 1 mL of sample was pipetted out every 15 min and centrifuged at 15000 rpm for 5 min followed by UV-Vis absorbance measurement of the supernatant. The same supernatant was used to re-suspend the Bac-FeOxNWs samples for further exposure. Measurements were taken every 15 minutes for total 3 h of illumination. Note that the experimental conditions were strictly controlled including the distance between the lamp and the sample vial (5 cm), the temperature of the vials (25-30 °C with a portable fan), the volume of the degradation solution (3 mL) and so on. A broad array of different parameters to optimize the photocatalytic properties of these novel natural visible-light photocatalyst nanowires were probed.

**2.5. Effect of Bac-FeOxNWs concentration.** The amount of photocatalyst plays a direct role in the degradation efficiency, and thus, we assessed five different concentrations (i.e. 0.1, 0.5, 1.0, 1.5, and 2.0 mg $mL^{-1}$) of all four types of Bac-FeOxNWs (i.e. Bac-FeOxNWs, Bac-FeOxNWs-600, Bac-FeOxNWs-800, and Bac-FeOxNWs-1000). This part of the study aimed to establish the optimal annealing temperature of the biofilm and corresponding concentration that provided the best photodegradation performance out of all the analyzed samples (i.e. 20 in this case). Note

that; further studies were carried out using the most efficient Bac-FeOxNWs sample determined by this part of our study (i.e. Bac-FeOxNWs-800 at 0.5 mg $mL^{-1}$). All the photodegradation experiments were carried out using the protocol defined above.

**2.6. Effect of initial concentration of Rhodamine B dye.** The starting concentration of the dye in the degradation solution has a great influence on the photodegradation performance due to varied adsorption/desorption kinetics. Therefore, we checked the effect of the initial dye concentration on the photodegradation properties of Bac-FeOxNWs-800 (i.e. the most efficient batch, 0.5 mg $mL^{-1}$). In a typical degradation experiment, a specific amount of Bac-FeOxNWs was suspended in 2940 µL of mili-Q water with 50 µL of dye stock solution (1mM) and incubated overnight in dark (*vide supra*). For investigating the effect of initial dye concentration, 10, 50and 100 µL of RhB (1 mM) were added to 2980, 2940, and 2890 µL of mili-Q water containing specific amount of Bac-FeOxNWs-800, respectively followed by addition of 10 µL of hydrogen peroxide, similar to previous degradation experiments to make the volume to 3 mL prior to exposure to visible light for photodegradation.

**2.7. Effect of pH on degradation of Rhodamine B.** The degradation of RhB under three different pH conditions (i.e. acidic: pH 3, neutral: pH 7, and basic: pH 9) was evaluated. For this, pH of mili-Q water was adjusted to the required values using 1M hydrochloric acid (HCl) or 1M sodium hydroxide (NaOH). Similar to previously defined degradation experiments, 2940 µL mili-Q water (with adjusted pH) and 50 µL of dye stock solution were added to a vial containing Bac-FeOxNWs-800 (0.5 mg $mL^{-1}$) and incubated overnight. Next day, 10 µL of hydrogen peroxide was added and the degradation was carried out as above by exposing the samples to white light for 3 h.

**2.8. Effect of additive on photodegradation of RhB.** Isopropanol was used in this part of the study to shine the light on the mechanism of degradation of this model dye by Bac-FeOxNWs. For this, Bac-FeOxNWs-800 were weighed (concentration 0.5 mg $mL^{-1}$) in a vial and suspended in 2940 µL of mili-Q water with 10 µL of isopropanol and 50 µL of dye stock solution (1mM). This suspension was incubated in dark overnight and subsequently exposed to white light as indicated in previous experiments.

## 3. RESULTS AND DISCUSSION

**3.1. Structure and morphology of Bac-FeOxNWs.** The SEM images of pristine bacteria nanowire (P-Bac-FeOxNWs) annealed at three different temperatures 600, 800 and 1000 °C in an air atmosphere for 1 hour are presented in **Figure 1**. These images revealed significant morphological changes were as a result of annealing process. The P-Bac-FeOxNWs (i.e. non-annealed nanowires) show a twisted helical-like structure composed of three or more nanowires with average length about 10 µm (**Figure 1a**). The average diameter of a single bacteria nanowire was measured to be approximately 139 ± 56 nm. Interestingly, the twisted helical structure of the nanowires progressively un-twirled after annealing at increasing temperatures. The SEM images of Bac-FeOxNWs-600, Bac-FeOxNWs 800, and Bac-FeOxNWs-1000 are presented in **Figures 1b, c, and d**, respectively. Also, the average length of the nanowires decreased from more than 10 µm to 400 nm with increasing annealing temperature going from 0 to 1000 °C (**Table 2**). Annealing at 600˚C resulted in fewer twists in the structure of the nanowires with a significant increase in surface roughness (**Figure 1b**). Annealing at 800 ˚C and 1000 °C reduced the twists further and also resulted in much higher surface roughness (**Figure 1c** and **Figure 1d**, respectively). The structural parameters and zeta potential of the Bac-

FeOxNWs after annealing at different temperatures are summarized in **Table 1**. TEM images of Bac-FeOxNWs is provided in **Figure S2** (Supporting information).

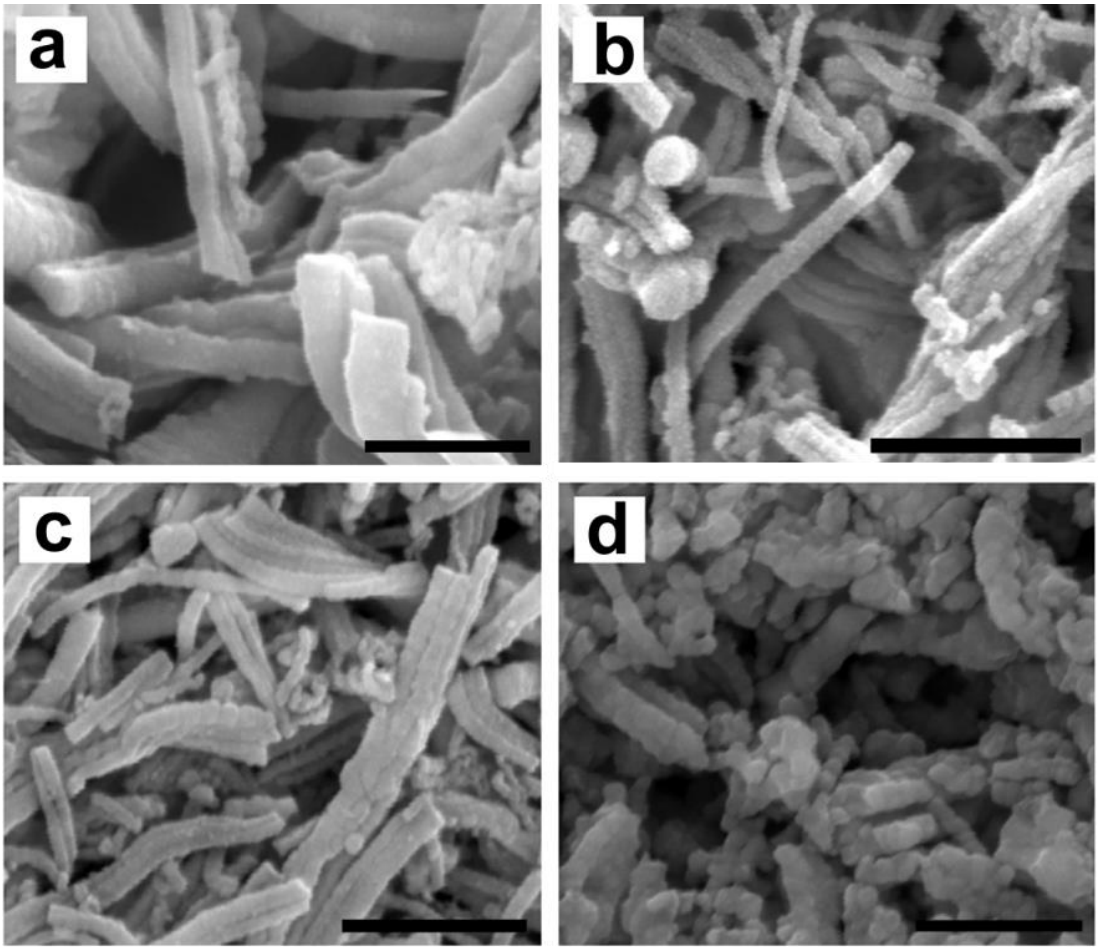


**Figure 1.** Scanning electron microscopy (SEM) images of Bac-FeOxNWs annealed at different temperatures: a) 25 °C (P-Bac-FeOxNWs), (b) 600 °C (Bac-FeOxNWs-600), (c) 800 °C (Bac-FeOxNWs-800), and (d) 1000 °C (Bac-FeOxNWs-1000). Scale bar for all the images is 1 µm.

**Table 1.** Summary of structural parameters, zeta potential, and BET surface area of Bac-FeOxNWs annealed at different temperatures.

| Annealing temperature (°C) | Sample name | Average length of Bac-FeOxNWs (µm) | Average diameter of Bac-FeOxNWs (nm) | Zeta potential (mV) | BET surface area ($m^2.g^{-1}$) |
|---|---|---|---|---|---|
| 25 | P-Bac-FeOxNWs | > 10.00 ± 2.78 | 208.59 ± 65.69 | - 24.1 | 6.72 |
| 600 | Bac-FeOxNWs-600 | 4.40 ± 1.82 | 117.14 ± 22.07 | - 23.4 | 9.97 |
| 800 | Bac-FeOxNWs-800 | 1.70 ± 0.92 | 99.80 ± 19.71 | -25.5 | 14.28 |
| 1000 | Bac-FeOxNWs-1000 | 0.40 ± 0.15 | 127.62 ± 22.98 | -21.7 | 16.44 |

**3.2. Chemical composition of Bac-FeOxNWs.** The chemical composition of Bac-FeOxNWs was investigated using IR spectroscopy, X-ray diffractometery, and Raman spectroscopy. The IR spectroscopy, presented in **Figure 2a**, shows a broad band associated with hydroxyl groups on the surface of Bac-FeOxNWs between 3000-3500 $cm^{-1}$, respectively. It is worth noticing that the peak assigned to Fe-O bond appears for samples annealed at 800 and 1000 °C at 441 and 524 $cm^{-1}$ (marked by blue and red lines). The crystal structure of the Bac-FeOxNWs was probed using X-Ray diffraction.[37-39] Initially, the P-Bac-FeOxNWs displayed no crystalline peaks but an amorphous phase of iron oxide. Nevertheless, the crystallinity of the nanowires increased with the annealing temperature. Bac-FeOxNWs-600 display negligible changes in the crystal structure, but distinct diffraction peaks appeared for Bac-FeOxNWs annealed at 800 and 1000 °C. The XRD spectrum suggests that the Bac-FeOxNWs were primarily composed of $Fe_2O_3$ (Hematite phase), especially the ones annealed at 800 °C and 1000 °C.[40-41]

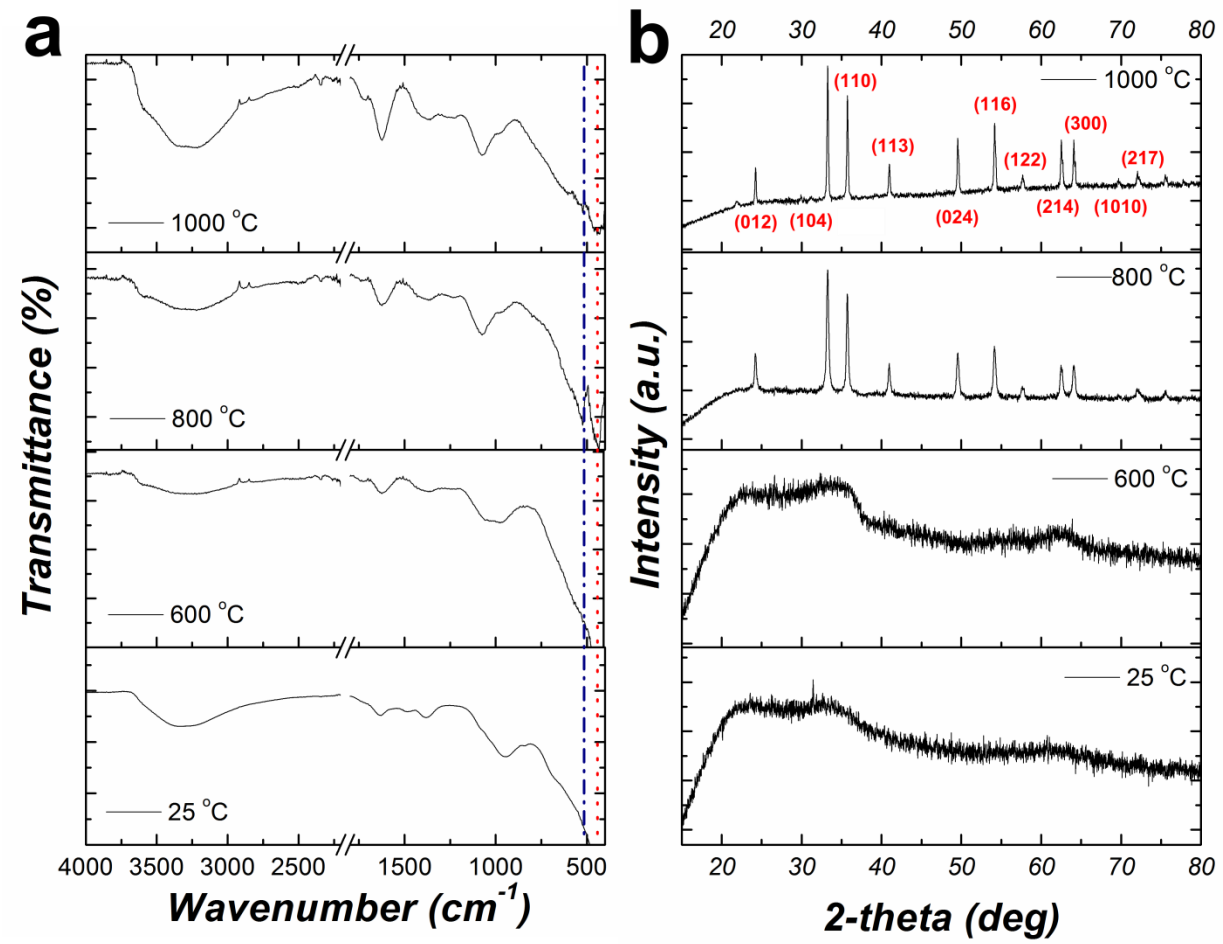


**Figure 2.** Chemical and crystallographic composition of Bac-FeOxNWs annealed at different temperatures determined by (a) FT-IR and (b) X-Ray diffractometry, note that the XRD peaks for both Bac-FeOxNWs-800 and Bac-FeOxNWs-1000 are the same, which are labeled in the top chart.

Raman spectroscopy analysis is corroborated in the X-ray diffraction results mentioned above, where no distinguishable peaks were observed for P-Bac-FeOxNWs and Bac-FeOxNWs-600, while Bac-FeOxNWs-800 and Bac-FeOxNWs-1000 showed peaks corresponding to $Fe_2O_3$ (**Figure S2a**, **Supporting Information**). The major Raman shifts bands (225.8, 246, 291.9, 409.2, 498.0 and 608.5 $cm^{-1}$) for Bac-FeOxNWs-800 and Bac-FeOxNWs-1000 were similar to

the Raman signature of Hematite α-$Fe_2O_3$ reported in the literature.[42-43] In addition, the energy dispersive X-ray (EDX) spectroscopy shows characteristic peaks assigned to iron and oxygen (**Figure S2b, Supporting Information**). The surface area plays a major role in adsorption and desorption of the RhB that governs the photocatalytic degradation process. Therefore, the surface area of Bac-FeOxNWs at all the annealing temperatures was determined using the nitrogen adsorption-desorption (**Table 1**).

The analysis of the magnetic properties of the iron oxide nanowires indicate that the peak saturation magnetization is observed for the samples annealed at 800 °C, showing a nearly single phase magnetic behaviour with an extraordinarily large coercivity (nearly 20 kOe) and the magnetic saturation almost 2 $emu.g^{-1}$ of Fe (**Figure S3, Supporting Information**). A video (**Video v1, Supporting Information**) provides further evidence of the strong magnetic properties of the iron oxide nanowires when exposed to an external magnetic field. This property could be readily used to recover these nanostructures after the photocatalytic process, which would minimize the impact of this catalyst on the environment.

### 3.2. Photocatalytic activity.

3.2.1. Effect of annealing temperature and initial Bac-FeOxNWs catalyst concentration.

The photocatalytic performance of Bac-FeOxNWs annealed at different temperatures was systematically assessed to optimize the initial amount of Bac-FeOxNWs using five concentrations (i.e. 0.1, 0.5, 1, 1.5, and 2 $mg.mL^{-1}$) with RhB as a model degradation molecule (**Figure 3**). The data shows that with increasing irradiation time, the amount of dye present in the sample decreases (monitored using UV-Vis spectroscopy), suggesting that both chromophores and aromatic rings of RhB have been destroyed (**Figure 3a**). **Figure 3a** provides time dependent

decrease in absorbance of RhB in the presence of 0.1 $mg.mL^{-1}$ of pristine Bac-FeOxNWs under visible light irradiation. Similar, time-dependent absorbance plots for Bac-FeOxNWs (0.5 $mg.mL^{-1}$) annealed at other temperatures (600, 800, and 1000°C) are provided in **Figure S4** (**Supporting information**). **Figure 3b** presents the amount of RhB left in the reaction mixture over a period of 180 min of irradiation for all the five concentration of pristine Bac-FeOxNWs. We found that the best degradation performance was achieved by pristine and Bac-FeOxNWs-600 at a concentration of 0.1 $mg.mL^{-1}$, with approximately 20 % of dye left after 3 h of visible light exposure. Similarly, **Figures 3c-e** show the time course of RhB degradation for all five concentrations of Bac-FeOxNWs annealed at 600, 800, and 1000 °C, respectively. Note that, the lower concentrations of Bac-FeOxNWs displayed better photodegradation capabilities in general for all the studied samples. However, 0.5 $mg.mL^{-1}$ of photocatalyst concentration was the most efficient in case of the samples annealed at 800 and 1000 °C. It is worth mentioning that the control experiment with same concentrations of Bac-FeOxNWs at all the annealing temperature did not result in significant degradation of the RhB under dark conditions (**Figure S5, Supporting Information**).

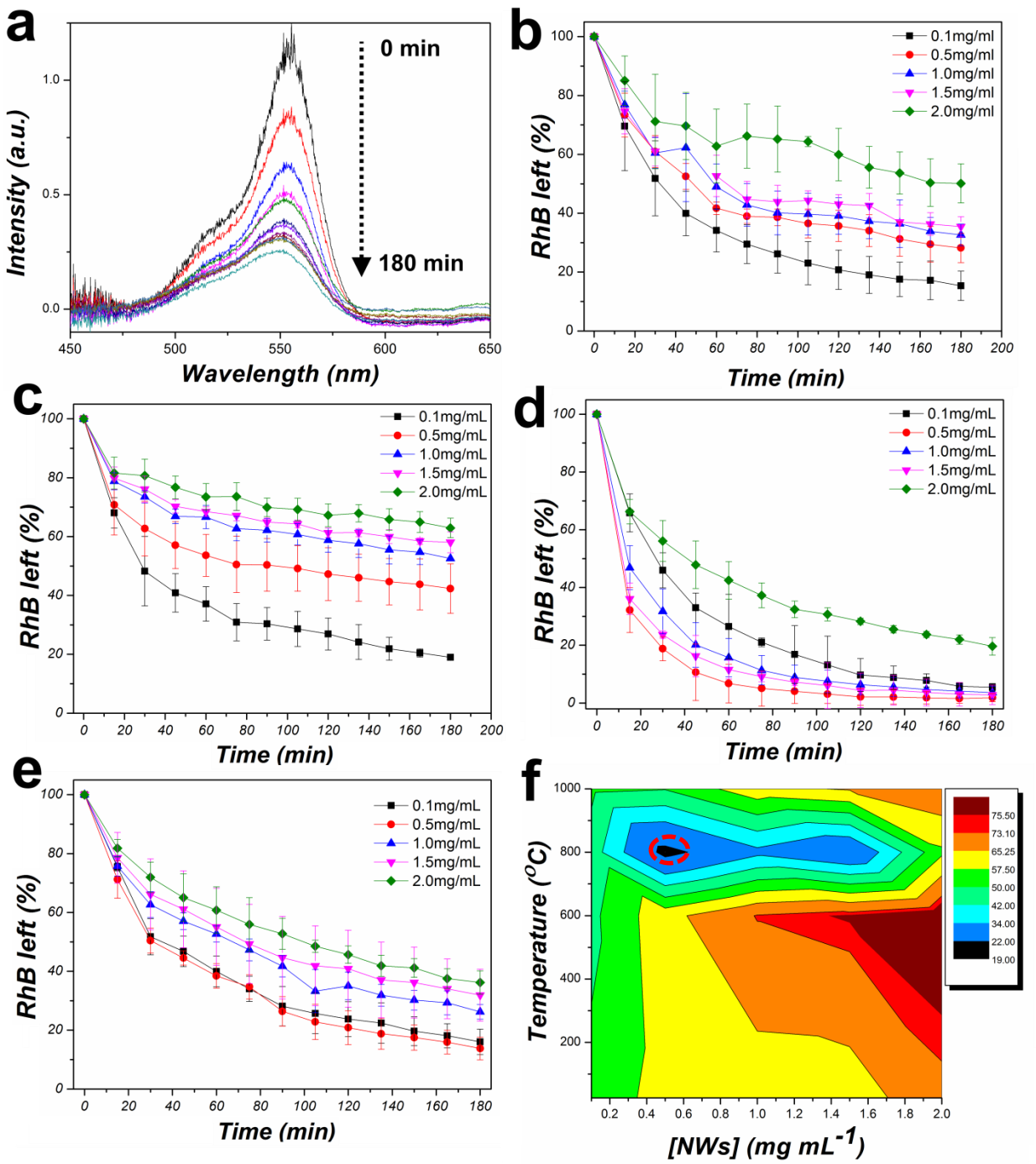


**Figure 3.** Photodegradation of RhB as a function of the irradiation time at different Bac-FeOxNWs concentrations and annealing temperatures. (a) UV-Vis spectrum of RhB at different time points of exposure to visible light in the presence of 0.1 mg.mL$^{-1}$ of pristine Bac-FeOxNWs. RhB left in the reaction mixture at different time points for five different concentrations of (b)

pristine Bac-FeOxNWs, (c) Bac-FeOxNWs-600, (d) Bac-FeOxNWs-800 and (e) Bac-FeOxNWs-1000. (f) Contour chart showing the relation between annealing temperature and concentration of Bac-FeOxNWs as a function of % RhB left after 30 min of visible light irradiation as indicated by the color chart on the right. The red circle points to the most optimal concentration and an annealing temperature of Bac-FeOxNWs for best performance.

The best photocatalytic performance at lower Bac-FeOxNWs concentrations (i.e. 0.1 and 0.5 $mg.mL^{-1}$) could be attributed to better and more efficient absorption of light (i.e. light penetration) and lower inter-particle exciton pair recombination. **Figure 3f** presents a contour chart summarizing the relation between the amounts of Bac-FeOxNWs and annealing temperature in terms of the amount of dye left after 30 min of visible light irradiation. The amount of dye left (%) is represented by different colors that are indicated by the color chart on the right of the contour plot. The Bac-FeOxNWs annealed at 800 °C at 0.5 $mg.mL^{-1}$ displayed the most eminent photocatalytic performance with almost 100 % RhB degradation in less than one hour. Therefore, a concentration of 0.5 $mg.mL^{-1}$ of iron oxide bacterial nanowires treated at 800 °C was used for all the further studies. We believe that this is due to two factors including clear crystalline structure and higher surface area of the Bac-FeOxNWs-800. It is also worth mentioning that although Bac-FeOxNWs-1000 displayed identical crystal structure, their surface area was measured to be much lower due to thermal aggregation/sintering.

3.2.2. Effect of initial dye concentration.

After establishing the most optimal annealing temperature and initial concentration of Bac-FeOxNWs for visible light photocatalysis, we studied the effect of the initial dye concentration on this process. Note that the Bac-FeOxNWs annealed at 800 °C (0.5 $mg.mL^{-1}$) were used for

this study with three initial dye concentrations (10, 50, and 100 µL of 1 mM RhB) in 3 mL of degradation solution, which is 0.33 x$10^{-5}$, 1.67 x $10^{-5}$, and 3.34 x $10^{-5}$ M of RhB. The results clearly show that the initial dye concentration had an effect on the efficiency of photocatalysis. The fastest photocatalysis is observed for 1.67 x $10^{-5}$ M of RhB in the degradation solution with the sample having 0.33 x $10^{-5}$ M of RhB closely following it, whereas the sample with 3.34 x $10^{-5}$ M of RhB degrades the slowest (**Figure 4**). In the case of 3.34 x $10^{-5}$ M of RhB, the poor photocatalytic performance is because large quantities of dye molecules were not adsorbed onto the Bac-FeOxNWs surface during dark overnight incubation. Also, the lifetime of the generated hydroxyl radicals is on the order of a few nanoseconds, and they can only react at or near the catalyst surface where they are formed. It is also believed that larger concentration of the dye tends to absorb a large portion of the irradiation light. Therefore, it is necessary to optimize the ratio of dye to nanoparticle photocatalyst. The poor photocatalysis performance of Bac-FeOxNWs with 10 µL is due to the lower amount of dye molecules, which leads to lower adsorption of dye molecules onto the Bac-FeOxNWs surface.

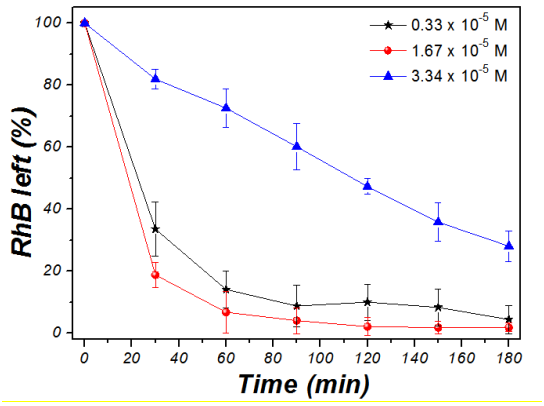


**Figure 4**. Time course of RhB degradation using 0.5 mg.mL$^{-1}$ of Bac-FeOxNWs-800 under visible light irradiation at a different initial concentration of RhB in the catalytic reaction mixture.

3.2.3. Effect of pH on visible light photocatalysis

The initial pH had a significant influence on the degradation of RhB by Bac-FeOxNWs photocatalyst (**Figure 5**). Clearly, the RhB degraded faster at acidic pH (i.e. pH 3.5) in comparison to neutral (i.e. pH 6.5) or basic (i.e. pH 8.5) pH ranges. At pH 3.5 almost all of the RhB degraded in less than 30 min, whereas at pH 7 more than 60 min were required for complete removal of RhB. Interestingly, at pH 8.5 there was approximately 12 % of the original amount of dye left in the solution after 3 hrs of irradiation. The reason for this is the significantly increased electrostatic interaction between Bac-FeOxNWs and RhB at lower pH. Under acidic pH conditions, Bac-FeOxNWs display a positive surface charge at acidic pH, because the iso-electric point of the hematite phase of iron oxide is around pH 8. RhB, on the other hand, has an iso-electric point at pH 3 and exists mainly as a neutral dye. Note that these results demonstrated that the RhB adsorption under dark is a significant step for photocatalysis.

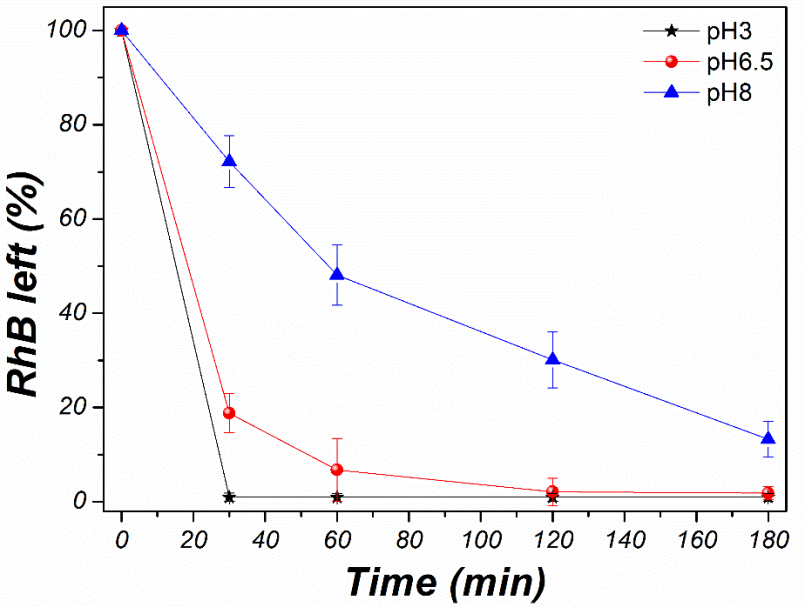


**Figure 5.** Time course of RhB degradation using 0.5 mg.mL$^{-1}$ of Bac-FeOxNWs-800 under visible light irradiation as a function of pH of the degradation mixture.

3.2.4. Reusability of Bac-FeOxNWs

We also evaluated the reusability of the magnetic nanowires based photocatalyst by repeated use of the same Bac-FeOxNWs sample for degradation of RhB. It is worth mentioning that the photocatalytic properties of the Bac-FeOxNWs do not show any obvious deterioration even after six consecutive cycles (**Figure 6**). This illustrates that the Bac-FeOxNWs are highly photostable over time. The photocatalytic stability are critical properties for many applications and has great potential in wastewater treatment and environmental remediation process. Furthermore, the structure of the reused Bac-FeOxNWs was analyzed using SEM, showing no morphological difference between freshly annealed Bac-FeOxNWs at 800 °C and a sample used as photocatalyst for six cycles (**Figure S6, Supporting Information**).

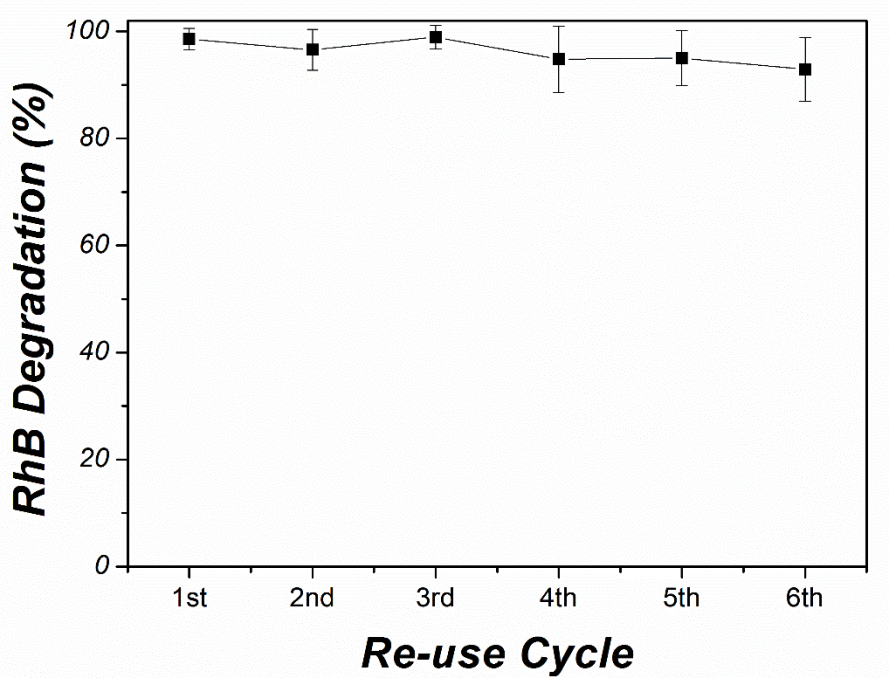


**Figure 6**. Reusability of the Bac-FeOxNWs photocatalyst (0.5 mg.mL$^{-1}$ of Bac-FeOxNWs-800) for degradation of RhB at a concentration of 1.67 10$^{-5}$ M under visible light irradiation for 2 h.

### 3.3. RhB degradation kinetics in the presence of Bac-FeOxNWs under visible light.

It is known that the photocatalytic degradation processes follow first order and Langmuir–Hinshelwood kinetics, which are given by the following equations, respectively:

$$r = -\frac{dC}{dt} = k_1 C \quad (1)$$

$$r = -\frac{dC}{dt} = \frac{K_{ad} k C}{1 + K_{ad} C} \quad (2)$$

According to the notion, $r$ is the rate of RhB degradation ($h^{-1}$ $mg.L^{-1}$), $C$ the concentration at time t ($mg.L^{-1}$), $k_1$ the first-order rate constant ($min^{-1}$), $K_{ad}$ the adsorption coefficient and $k$ is the reaction rate constant. Integrating the eq (1) with limits C= $C_0$ at t=0 and C=C at t=t provides the non-linear form of first order kinetics (3).

$$C = C_0 e^{-k_1 t} \quad (3)$$

Assuming negligible adsorption of dye onto Bac-FeOxNWs, the LH model can be rewritten as first-order kinetics equation, which has been previously demonstrated by many groups.[15, 44-47]

Therefore, the photo-reactivity of iron oxide nanowires with RhB was evaluated by fitting the degradation data to a first-order reaction kinetic model (**Table 2**). In terms of annealing temperature and concentration of Bac-FeOxNWs the highest first order rate constant was recorded for the sample annealed at 800 °C (0.5 $mg.mL^{-1}$) having an apparent reaction rate constant of $k = 4.19 \times 10^{-2}\ min^{-1}$ validating our experimental results. Similarly, rate constants for different initial dye concentration of $0.33 \times 10^{-5}$, $1.67 \times 10^{-5}$, and $3.34 \times 10^{-5}$ M (in the degradation mixture) were found to be $1.79 \times 10^{-2}\ min^{-1}$ , $4.19 \times 10^{-2}\ min^{-1}$, and $1.22 \times 10^{-2}\ min^{-1}$, respectively (**Table 3**).

**Table 2.** Reaction rate-constant for Bac-FeOxNWs annealed at four different temperatures and five different initial Bac-FeOxNWs concentrations in the degradation mixture with fixed RhB concentration ($1.67 \times 10^{-5}$ M).

| Annealing temperature (°C) | Bac-FeOxNWs Concentration (mg.mL$^{-1}$) | $k_1$ (x $10^{-2}$ min$^{-1}$) | $R^2$ |
|---|---|---|---|
| pristine | 0.1 | 2.23 | 0.99 |
| | 0.5 | 1.80 | 0.95 |
| | 1.0 | 2.05 | 0.95 |
| | 1.5 | 2.12 | 0.86 |
| | 2.0 | 2.17 | 0.67 |
| 600°C | 0.1 | 1.98 | 0.95 |
| | 0.5 | 1.80 | 0.95 |
| | 1.0 | 1.54 | 0.97 |
| | 1.5 | 2.19 | 0.87 |
| | 2.0 | 1.43 | 0.97 |
| 800°C | 0.1 | 2.83 | 0.93 |
| | 0.5 | 4.19 | 0.98 |
| | 1.0 | 2.76 | 0.99 |
| | 1.5 | 2.97 | 0.96 |
| | 2.0 | 1.87 | 0.98 |
| 1000°C | 0.1 | 2.10 | 0.99 |
| | 0.5 | 2.03 | 0.99 |
| | 1.0 | 1.89 | 0.97 |
| | 1.5 | 1.91 | 0.98 |
| | 2.0 | 1.98 | 0.91 |

**Table 3.** First order RhB degradation rate-constant as a function of initial RhB concentration in the degradation mixture.

| RhB concentration (x$10^{-5}$ M) | Bac-FeOxNWs Concentration (mg.mL$^{-1}$) | $k_1$ (x $10^{-2}$ min$^{-1}$) | $R^2$ |
|---|---|---|---|
| 0.33 | 0.5 | 1.80 | 0.83 |
| 1.67 | 0.5 | 4.19 | 0.98 |
| 3.34 | 0.5 | 1.22 | 0.98 |

### 3.4. Mechanism of Photocatalytic activity of Bac-FeOxNWs.

The mechanism of RhB degradation using iron oxide nanowires could either be due to high energy valence band holes or OH radicals, which was discerned by using hydrogen peroxide and isopropanol as additives. Hydrogen peroxide and isopropanol were intentionally chosen based on the ability of production of hydroxyl radicals of hydrogen peroxide and, on the other hand, isopropyl alcohol for its high reaction rate constant with the hydroxyl radicals ($1.9 \times 10^9$ L mol$^{-1}$ s$^{-1}$) (i.e. quenching of hydroxyl radicals). **Figure 7** shows that the degradation of RhB is faster and more efficient in the presence of hydrogen peroxide, whereas it becomes slower and less efficient in the presence on isopropanol. Based on the results presented in **Figure 7**, it is clear that the photocatalytic reaction proceeds according to the following chemical equations.

$$\alpha\, Fe_2O_3 \rightarrow\ Fe_2O_3\ (e^- + h^+) \qquad 4$$

$$H_2O_2 + e^- \rightarrow OH^- + OH^{\cdot} \qquad 5$$

Or

$$H_2O + h^+ \rightarrow H^+ + OH^{\cdot} \qquad 6$$

$$2H_2O + 2h^+ \rightarrow H_2O_2 + 2H^+ \qquad 7$$

$$H_2O_2 \rightarrow 2\, OH^{\cdot} \qquad 8$$

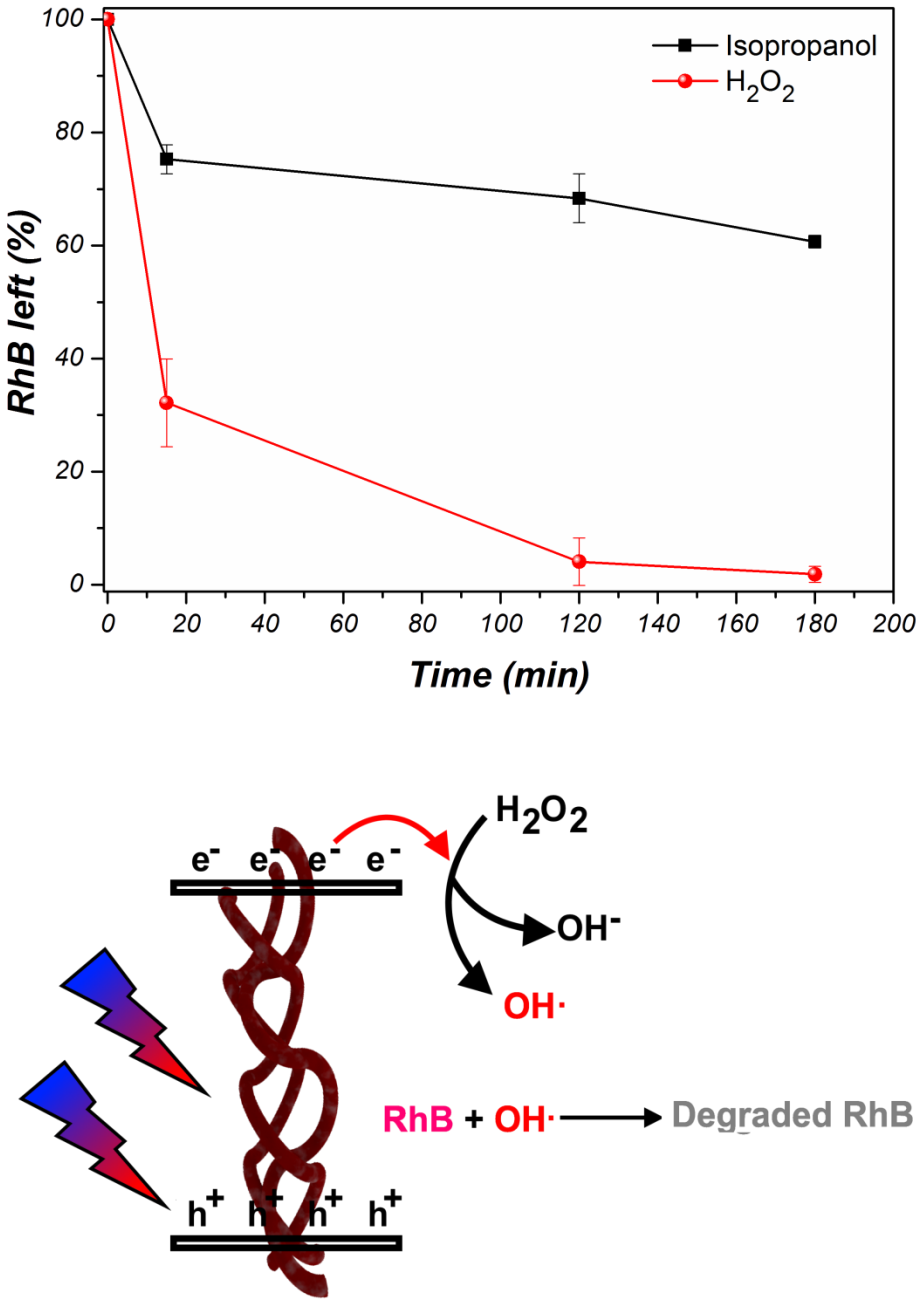


**Figure 7.** Effect of addition of isopropyl alcohol and hydrogen peroxide on the photocatalytic degradation of RhB with 0.5 mg.mL$^{-1}$ of Bac-FeOxNWs-800 and 1.67 10$^{-5}$ M RhB. (b) A schematic showing the proposed photocatalytic process for efficient degradation of RhB using Bac-FeOxNWs photocatalyst under visible light irradiation.

### 3.5. Comparison of photocatalytic activity with other iron oxide nanomaterials.

Recently, a plethora of studies have been aimed at investigating and exploring different iron oxide and magnetic materials for photocatalysis applications. Therefore, it is necessary to provide a comparison with key studies and highlight their advantages. **Table 4** provides a comparison matrix summarizing the photocatalytic activity of different iron oxide materials and their composites used in degradation of organic dyes (especially Rhodamine B). Since the production of these synthetic nanomaterials results in generation of toxic and polluting waste, it nullifies their significance for waste water treatment. Naturally produced functional nanostructures offer a significant advantage in this scenario as presented in this report. The iron oxide nanowires photocatalysts utilized in this report were obtained as biofilm waste from River Murray water system in South Australia. This waste material requires minor and low-cost processing to be used at the level required for industrial efficient visible-light photocatalyst.

**Table 4.** A table summarizing the properties of the different types of photocatalyst used for degradation of Rhodamine B under visible light irradiation and their key problem.

| Shape and Composition of the material | Initial Dye concentration (M) | Degradation time (min) | Remarks | [Ref] |
|---|---|---|---|---|
| **Spherical nanoparticles, $Fe_3O_4$@$SiO_2$@AgCl : Ag** | $1.04 \times 10^{-5}$ | 5 | 300 W lamp, expensive starting material with complicated synthesis process | [16] |
| **Spherical nanoparticels, Ag–AgI/$Fe_3O_4$@$SiO_2$** | $5.20 \times 10^{-5}$ | 60-80 | 250 W lamp, expensive starting material with complicated synthesis process | [17] |
| **Nanosized Sheets, $Bi_2WO_6$** | $2 \times 10^{-4}$ | ~60 | 500 W lamp, large amounts of catalyst required 200 mg | [19] |

| | | | | |
|---|---|---|---|---|
| | | | for 200 mL of RhB solution | |
| **Micro and nano rods, α-Fe2O3 and α-FeOOH** | 2 x $10^{-5}$ | 40-180 | 300 W lamp, expensive and complicated synthesis process | [22] |
| **Nanowires, α-$Fe_2O_3$** | 1.67 x $10^{-5}$ | 45-60 | 150 W lamp, Inexpensive and naturally produced biofilm waste, abundantly available, and easy processing | This work |

## 4. CONCLUSIONS

In this work, we have demonstrated for the first time the use of naturally derived iron oxide based 1-d nanostructure in the form of nanowires as highly efficient visible-light photocatalyst. The narrow band-gap of the iron oxide in combination with the high surface area of these bacterial nanowires leads to an enhanced optical absorption and generation of exciton pairs, providing unprecedented Rhodamine B degradation efficiency. We investigated the effect of annealing temperature on the structure and photocatalytic efficiency of these nanowires. Annealing at 800 °C converted the amorphous iron oxide nanowires into α-$Fe_2O_3$ that provided the best catalytic activity, degrading RhB (1.7 $10^{-5}$ M) completely in less than an hour. This work also provides detailed insights into the effect of various other parameters such as the initial concentration of RhB and iron oxide nanowires in the degradation mixture, pH, and additives such as hydrogen peroxide and isopropyl alcohol. It is also worth mentioning that this naturally produced iron oxide nanowires based photocatalyst were reused 6 times without evident loss of activity. The low cost of production, high photocatalytic activity, stability, magnetic activity, and high surface area make these nanowires a promising material in environmental remediation and industrial catalysis applications.

ASSOCIATED CONTENT

**Supporting Information**

The supporting information file provides further details about chemical and magnetic characterization with Raman spectrum and superconducting quantum interference device (SQUID) magneto gram. Time dependent UV-Visible spectrum of Rhodamine B degradation in presence of iron oxide nanowires under visible light irradiation. SEM image of Bac-FeOxNWs after 6 re-use cycles. This material is available free of charge via the internet at http://pubs.acs.org.

AUTHOR INFORMATION

**Corresponding Author**

*E-mail: dusan.losic@adelaide.edu.au

* E-mail: mlambert@civeng.adelaide.edu.au

**Author Contributions**

The manuscript was written through contributions of all authors. All authors have given approval to the final version of the manuscript.

**Notes**

§ These authors contributed equally to this work.

ACKNOWLEDGEMENTS

Authors acknowledge the financial support provided by the Australian Research Council (FT 110100711) and the School of Chemical Engineering – The University of Adelaide. We thank the workshop staff from the School of Chemical Engineering, particularly, Mr. Jason Peak, Mr. Michael Jung, and Mr. Jeffrey Hiorns for assistance with the Photocatalysis setup.

REFERENCE

1. Fox, M. A.; Dulay, M. T., Heterogeneous photocatalysis. *Chemical reviews* **1993,** *93* (1), 341-357.
2. Fujishima, A.; Rao, T. N.; Tryk, D. A., Titanium dioxide photocatalysis. *Journal of Photochemistry and Photobiology C: Photochemistry Reviews* **2000,** *1* (1), 1-21.
3. Fujishima, A., Electrochemical photolysis of water at a semiconductor electrode. *nature* **1972,** *238*, 37-38.
4. Fox, M.; Dulay, M., Acceleration of secondary dark reactions of intermediates derived from adsorbed dyes on irradiated TiO 2 powders. *Journal of Photochemistry and Photobiology A: Chemistry* **1996,** *98* (1), 91-101.
5. Subramanian, V.; Wolf, E.; Kamat, P. V., Semiconductor-metal composite nanostructures. To what extent do metal nanoparticles improve the photocatalytic activity of TiO2 films? *The Journal of Physical Chemistry B* **2001,** *105* (46), 11439-11446.
6. Chen, X.; Liu, L.; Peter, Y. Y.; Mao, S. S., Increasing solar absorption for photocatalysis with black hydrogenated titanium dioxide nanocrystals. *Science* **2011,** *331* (6018), 746-750.
7. Burda, C.; Lou, Y.; Chen, X.; Samia, A. C.; Stout, J.; Gole, J. L., Enhanced nitrogen doping in TiO2 nanoparticles. *Nano letters* **2003,** *3* (8), 1049-1051.
8. Peng, T.; Zhao, D.; Dai, K.; Shi, W.; Hirao, K., Synthesis of titanium dioxide nanoparticles with mesoporous anatase wall and high photocatalytic activity. *The Journal of Physical Chemistry B* **2005,** *109* (11), 4947-4952.
9. Asahi, R.; Morikawa, T.; Ohwaki, T.; Aoki, K.; Taga, Y., Visible-light photocatalysis in nitrogen-doped titanium oxides. *Science* **2001,** *293* (5528), 269-271.
10. Momeni, M. M.; Ghayeb, Y., Fabrication, characterization and photocatalytic properties of Au/TiO2-WO3 nanotubular composite synthesized by photo-assisted deposition and electrochemical anodizing methods. *Journal of Molecular Catalysis A: Chemical* **2016,** *417*, 107-115.
11. Momeni, M. M.; Ghayeb, Y., Cobalt modified tungsten–titania nanotube composite photoanodes for photoelectrochemical solar water splitting. *Journal of Materials Science: Materials in Electronics* **2016,** *27* (4), 3318-3327.
12. Momeni, M. M., Fabrication of copper decorated tungsten oxide–titanium oxide nanotubes by photochemical deposition technique and their photocatalytic application under visible light. *Applied Surface Science* **2015,** *357*, 160-166.
13. Zong, X.; Sun, C.; Yu, H.; Chen, Z. G.; Xing, Z.; Ye, D.; Lu, G. Q.; Li, X.; Wang, L., Activation of photocatalytic water oxidation on N-doped ZnO bundle-like nanoparticles under visible light. *The Journal of Physical Chemistry C* **2013,** *117* (10), 4937-4942.

14. Cao, C.; Xiao, L.; Chen, C.; Cao, Q., Magnetically separable $Cu_2O$/chitosan–$Fe_3O_4$ nanocomposites: preparation, characterization and visible-light photocatalytic performance. *Applied Surface Science* **2015,** *333*, 110-118.
15. Wang, X. H.; Li, J. G.; Kamiyama, H.; Moriyoshi, Y.; Ishigaki, T., Wavelength-Sensitive Photocatalytic Degradation of Methyl Orange in Aqueous Suspension over Iron(III)-doped $TiO_2$ Nanopowders under UV and Visible Light Irradiation. *The Journal of Physical Chemistry B* **2006,** *110* (13), 6804-6809.
16. Wang, D.-H.; Jia, L.; Wu, X.-L.; Lu, L.-Q.; Xu, A.-W., One-step hydrothermal synthesis of N-doped $TiO_2$/C nanocomposites with high visible light photocatalytic activity. *Nanoscale* **2012,** *4* (2), 576-584.
17. Pradhan, G. K.; Martha, S.; Parida, K., Synthesis of multifunctional nanostructured zinc–iron mixed oxide photocatalyst by a simple solution-combustion technique. *ACS applied materials & interfaces* **2012,** *4* (2), 707-713.
18. Yu, H.; Cao, G.; Chen, F.; Wang, X.; Yu, J.; Lei, M., Enhanced photocatalytic performance of $Ag_3PO_4$ by simutaneous loading of Ag nanoparticles and Fe(III) cocatalyst. *Applied Catalysis B: Environmental* **2014,** *160–161*, 658-665.
19. Yao, Y. R.; Huang, W. Z.; Zhou, H.; Cui, X.; Zheng, Y. F.; Song, X. C., Synthesis of core–shell nanostructured magnetic photocatalyst Fe3O4@SiO2@Ag3PO4 with excellent visible-light-responding photocatalytic activity. *Journal of Nanoparticle Research* **2014,** *16* (11), 1-10.
20. Xu, J.-W.; Gao, Z.-D.; Han, K.; Liu, Y.; Song, Y.-Y., Synthesis of Magnetically Separable Ag3PO4/TiO2/Fe3O4 Heterostructure with Enhanced Photocatalytic Performance under Visible Light for Photoinactivation of Bacteria. *ACS applied materials & interfaces* **2014,** *6* (17), 15122-15131.
21. Momeni, M. M.; Ghayeb, Y., Fabrication, characterization and photoelectrochemical behavior of Fe–TiO2 nanotubes composite photoanodes for solar water splitting. *Journal of Electroanalytical Chemistry* **2015,** *751*, 43-48.
22. Liu, Y.; Yu, L.; Hu, Y.; Guo, C.; Zhang, F.; Lou, X. W. D., A magnetically separable photocatalyst based on nest-like γ-Fe 2 O 3/ZnO double-shelled hollow structures with enhanced photocatalytic activity. *Nanoscale* **2012,** *4* (1), 183-187.
23. An, C.; Ming, X.; Wang, J.; Wang, S., Construction of magnetic visible-light-driven plasmonic Fe 3 O 4@ SiO 2@ AgCl: Ag nanophotocatalyst. *Journal of Materials Chemistry* **2012,** *22* (11), 5171-5176.
24. Guo, J.-F.; Ma, B.; Yin, A.; Fan, K.; Dai, W.-L., Photodegradation of rhodamine B and 4-chlorophenol using plasmonic photocatalyst of Ag–AgI/Fe 3 O 4@ SiO 2 magnetic nanoparticle under visible light irradiation. *Applied Catalysis B: Environmental* **2011,** *101* (3), 580-586.
25. Wang, Y.; Li, S.; Xing, X.; Huang, F.; Shen, Y.; Xie, A.; Wang, X.; Zhang, J., Self‐Assembled 3D Flowerlike Hierarchical Fe3O4@ Bi2O3 Core–Shell Architectures and Their Enhanced Photocatalytic Activity under Visible Light. *Chemistry–A European Journal* **2011,** *17* (17), 4802-4808.
26. Fu, H.; Pan, C.; Yao, W.; Zhu, Y., Visible-light-induced degradation of rhodamine B by nanosized Bi2WO6. *The Journal of Physical Chemistry B* **2005,** *109* (47), 22432-22439.
27. Seabold, J. A.; Choi, K.-S., Efficient and Stable Photo-Oxidation of Water by a Bismuth Vanadate Photoanode Coupled with an Iron Oxyhydroxide Oxygen Evolution Catalyst. *Journal of the American Chemical Society* **2012,** *134* (4), 2186-2192.
28. Zhu, X.; Hang, Q.; Xing, Z.; Yang, Y.; Zhu, J.; Liu, Z.; Ming, N.; Zhou, P.; Song, Y.; Li, Z., Microwave Hydrothermal Synthesis, Structural Characterization, and Visible‐Light Photocatalytic Activities of Single‐Crystalline Bismuth Ferric Nanocrystals. *Journal of the American Ceramic Society* **2011,** *94* (8), 2688-2693.
29. Singaravelu, G.; Arockiamary, J. S.; Kumar, V. G.; Govindaraju, K., A novel extracellular synthesis of monodisperse gold nanoparticles using marine alga, Sargassum wightii Greville. *Colloids and Surfaces B: Biointerfaces* **2007,** *57* (1), 97-101.

30. Bharde, A. A.; Parikh, R. Y.; Baidakova, M.; Jouen, S.; Hannoyer, B.; Enoki, T.; Prasad, B.; Shouche, Y. S.; Ogale, S.; Sastry, M., Bacteria-mediated precursor-dependent biosynthesis of superparamagnetic iron oxide and iron sulfide nanoparticles. *Langmuir* **2008,** *24* (11), 5787-5794.
31. Huang, J.; Li, Q.; Sun, D.; Lu, Y.; Su, Y.; Yang, X.; Wang, H.; Wang, Y.; Shao, W.; He, N., Biosynthesis of silver and gold nanoparticles by novel sundried Cinnamomum camphora leaf. *Nanotechnology* **2007,** *18* (10), 105104.
32. Xie, J.; Lee, J. Y.; Wang, D. I.; Ting, Y. P., Identification of active biomolecules in the high‐yield synthesis of single‐crystalline gold nanoplates in algal solutions. *small* **2007,** *3* (4), 672-682.
33. Arockiya Aarthi Rajathi, F.; Parthiban, C.; Ganesh Kumar, V.; Anantharaman, P., Biosynthesis of antibacterial gold nanoparticles using brown alga, Stoechospermum marginatum (kützing). *Spectrochimica Acta Part A: Molecular and Biomolecular Spectroscopy* **2012,** *99*, 166-173.
34. Narayanan, K. B.; Sakthivel, N., Biological synthesis of metal nanoparticles by microbes. *Advances in Colloid and Interface Science* **2010,** *156* (1–2), 1-13.
35. Singer, E.; Emerson, D.; Webb, E. A.; Barco, R. A.; Kuenen, J. G.; Nelson, W. C.; Chan, C. S.; Comolli, L. R.; Ferriera, S.; Johnson, J., Mariprofundus ferrooxydans PV-1 the first genome of a marine Fe (II) oxidizing Zetaproteobacterium. *PloS one* **2011,** *6* (9), e25386.
36. Singer, E.; Heidelberg, J. F.; Dhillon, A.; Edwards, K. J., Metagenomic insights into the dominant Fe (II) oxidizing Zetaproteobacteria from an iron mat at Lo'ihi, Hawai'i. *Front. Microbiol* **2013,** *4* (52), 10.3389.
37. Bharath, G.; Ponpandian, N., Hydroxyapatite nanoparticles on dendritic α-Fe 2 O 3 hierarchical architectures for a heterogeneous photocatalyst and adsorption of Pb (ii) ions from industrial wastewater. *RSC Advances* **2015,** *5* (103), 84685-84693.
38. Bharath, G.; Prabhu, D.; Mangalaraj, D.; Viswanathan, C.; Ponpandian, N., Facile in situ growth of Fe 3 O 4 nanoparticles on hydroxyapatite nanorods for pH dependent adsorption and controlled release of proteins. *RSC Advances* **2014,** *4* (92), 50510-50520.
39. Zhou, X.; Yang, H.; Wang, C.; Mao, X.; Wang, Y.; Yang, Y.; Liu, G., Visible Light Induced Photocatalytic Degradation of Rhodamine B on One-Dimensional Iron Oxide Particles†. *The Journal of Physical Chemistry C* **2010,** *114* (40), 17051-17061.
40. Han, R.; Li, W.; Pan, W.; Zhu, M.; Zhou, D.; Li, F.-s., 1D Magnetic materials of Fe3O4 and Fe with high performance of microwave absorption fabricated by electrospinning method. *Scientific reports* **2014,** *4*.
41. Yin, Y.; Zeng, M.; Liu, J.; Tang, W.; Dong, H.; Xia, R.; Yu, R., Enhanced high-frequency absorption of anisotropic Fe3O4/graphene nanocomposites. *Scientific reports* **2016,** *6*, 25075.
42. Chaudhari, N.; Warule, S.; Muduli, S.; Kale, B.; Jouen, S.; Lefez, B.; Hannoyer, B.; Ogale, S., Maghemite (hematite) core (shell) nanorods via thermolysis of a molecular solid of Fe-complex. *Dalton Transactions* **2011,** *40* (31), 8003-8011.
43. Froment, F.; Tournié, A.; Colomban, P., Raman identification of natural red to yellow pigments: ochre and iron‐containing ores. *Journal of Raman Spectroscopy* **2008,** *39* (5), 560-568.
44. Chakrabarti, S.; Dutta, B. K., Photocatalytic degradation of model textile dyes in wastewater using ZnO as semiconductor catalyst. *Journal of Hazardous Materials* **2004,** *112* (3), 269-278.
45. Behnajady, M. A.; Modirshahla, N.; Hamzavi, R., Kinetic study on photocatalytic degradation of C.I. Acid Yellow 23 by ZnO photocatalyst. *Journal of Hazardous Materials* **2006,** *133* (1–3), 226-232.
46. Emeline, A. V.; Ryabchuk, V.; Serpone, N., Factors affecting the efficiency of a photocatalyzed process in aqueous metal-oxide dispersions: Prospect of distinguishing between two kinetic models. *Journal of Photochemistry and Photobiology A: Chemistry* **2000,** *133* (1–2), 89-97.
47. Vasanth Kumar, K.; Porkodi, K.; Selvaganapathi, A., Constrain in solving Langmuir–Hinshelwood kinetic expression for the photocatalytic degradation of Auramine O aqueous solutions by ZnO catalyst. *Dyes and Pigments* **2007,** *75* (1), 246-249.